Fracture roughness and gouge distribution of a granite shear band

David Amitrano
Laboratoire Environnement Géomécanique et Ouvrages, Ecole Nationale Supérieure des Mines de Nancy, Nancy, France

Jean Schmittbuhl
Laboratoire de Géologie, Ecole Normale Supérieure de Paris, Paris, France

Received 14 January 2002; revised 11 June 2002; accepted 29 July 2002; published 28 December 2002.

[1] Localization of deformation during fracture mechanical tests leads to the development of shear bands. We performed triaxial tests using Sidobre granite at four different confining pressures (from 20 to 80 MPa). We compared two sets of tests: one set was stopped immediately after the formation of the shear band; a second one included additional shear deformation. From the analysis of thin sections of these laboratory samples, we characterize the typical microstructures in the shear band (mode I and II cracks, Riedel cracks, cataclastic flow). Statistical properties of rupture surface roughness and gouge grain size reveals scaling invariance. Using a mechanical profiler, the fracture roughness is measured along parallel profiles and shown to be correctly described over up to 3 orders of magnitude by self-affine geometry with a roughness exponent close to $\zeta = 0.80$. This property is very similar to tensile crack even if local processes are different. The influence of the slip is observed. Fracture surfaces are rougher along the slip direction ($\zeta = 0.74$) than perpendicular to it ($\zeta^* = 0.80$). The confining pressure is shown to have a weak effect on the fracture roughness. It smoothes the surface: slight increase of the roughness exponent. Gouge particles extracted from the shear band present a power law distribution with an exponent ranging from 1.44 to 1.91. This exponent appears to increase with the shearing displacement and the confining pressure. When a significant shear of the band is combined with a high confining pressure (i.e., impeded dilation of the band), the hallmark of fragmentation is observed for the particle distribution and related to a smoothing of the band boundary. *INDEX TERMS:* 5104 Physical Properties of Rocks: Fracture and flow; 5112 Physical Properties of Rocks: Microstructure; 8010 Structural Geology: Fractures and faults; 8020 Structural Geology: Mechanics; *KEYWORDS:* fracture, roughness, gouge, self-affinity

Citation: Amitrano, D., and J. Schmittbuhl, Fracture roughness and gouge distribution of a granite shear band, *J. Geophys. Res.*, *107*(B12), 2375, doi:10.1029/2002JB001761, 2002.

1. Introduction

[2] Deformation of rocks, when loaded at high strain rate and low temperature involves damage processes such as microfracturing [*Kranz*, 1983; *King and Sammis*, 1992]. During the first steps of the loading of initially intact rocks, microfracturing appears to be homogeneously distributed in the whole material. As microfracturing progresses, cooperative interactions of cracks take place and lead to the coalescence of microcracks and the initiation of a macroscopic fracture [*Costin*, 1983; *Kranz*, 1983; *Reches and Lockner*, 1994; *Schulson et al.*, 1999]. Such coalescence process has been experimentally observed by acoustic emission source location [*Lockner et al.*, 1991]. After failure, or when the discontinuity already exists, deformation is localized along the rupture band.

0148-0227/02/2002JB001761$09.00

[3] Low-scale observations reveal that the rupture zone or shear band is made of a granular material (i.e., gouge or cataclasis), in-filled between two rupture surfaces. The different aspects of damage: cracks, rupture surface, gouge, that result from the deformation process, can be observed either at the field scale (natural faults) or at the laboratory sample scale [e.g., *Keller et al.*, 1997; *Wibberley et al.*, 2000]. Shear deformation occurs both on the rupture surface and within the gouge layer involving friction surface erosion [e.g., *Wang and Scholz*, 1994] and grain fracturing [e.g., *Michibayashi*, 1996; *Biarez and Hicher*, 1997]. The latter reduces particle size as shear progresses. Thin particles might form subshear bands as observed both at laboratory scale or at field scale [*Moore et al.*, 1989; *Menendez et al.*, 1996; *Lin*, 1999; *Mair et al.*, 2000].

[4] Each aspect of the damage process during fracturing reveals scaling invariances [*King and Sammis*, 1992; *Turcotte*, 1992]. Power law scaling is found for: crack lengths, crack spatial distributions [*Hirata et al.*, 1987; *Velde et al.*,

1993], rupture surface roughness [*Brown and Scholz*, 1985; *Schmittbuhl et al.*, 1993, 1995b; *Bouchaud*, 1997], and grain-size distribution of the gouge [*Sammis and Biegel*, 1989; *Marone and Scholz*, 1989; *Weiss and Gay*, 1998].

[5] Particle size distributions of natural fault gouges have revealed power law distributions over the range 5 μm to 1 cm in agreement with a fractal geometry of fragmented material [*Sammis and Biegel*, 1989]. The upper and lower fractal cutoff scales appear to be related to the shearing displacement and the mineral constitution [*Weiss and Gay*, 1998]. Power law exponents, i.e., fractal dimensions, observed for natural fragmented objects range from 1.4 to 3 [*Turcotte*, 1992] depending on the rock type and on the fragmentation process [*Blenkinsop and Fernandes*, 2000; *Suteanu et al.*, 2000; *Hecht*, 2000].

[6] The mechanical behavior of rock discontinuities has been addressed using different approaches according to the morphology of the shear zone: flat or rough surfaces, and with or without in-filling material of various thicknesses. One of the most common approaches to describe the mechanical response of the discontinuity is the characterization of an interface law, i.e., a constitutive law [*Dieterich*, 1979; *Ruina*, 1983; *Marone*, 1998]. Such a description implicitly assumes that the interface is flat with no thickness. It is a phenomenological description with little information on the exact microstructure. State variables attempt to account for interfacial processes like healing, asperity strain or roughness history.

[7] Another approach is to consider a rough surface without in-filling material. For quantitative estimates of the rock surface morphology (angularity, roughness magnitude, asperity heights, roughness degradation during shearing), numerous authors [e.g., *Barton and Choubey*, 1977; *Hoek*, 1983; *Yu and Vayssade*, 1991; *Belem et al.*, 2000] proposed parameters which are included in constitutive laws of sheared rock joints (see *Homand et al.* [2001] for a review). The main problem of this approach is that the roughness parameters are scale-dependent and consequently the parameters estimated from laboratory samples cannot be used to describe larger-scale fractures such as natural faults. Moreover it does not take into account the scale effect observed for the shear strength of rock surfaces (the strength decreases as the scale increases [see *Barton and Choubey,* 1977]). *Sakellariou et al.* [1991] proposed that this scale effect could be explained by the self-affine property of rock surfaces. Self-affinity implies that the surface appears less rough as the scale increases. Accordingly, the shear strength of rock fractures decreases as the roughness decreases, or as the scale increases.

[8] Evidence of the mechanical effects of in-filling granular material on joint shearing have been obtained from laboratory tests. Several experimental works have been performed introducing a gouge layer between two cut blocks to simulate fault behavior [e.g., *Marone and Scholz*, 1989; *Moore et al.*, 1989; *Karner and Marone*, 1998; *Sleep et al.*, 2000]. Constitutive laws that include state variables (e.g., gouge thickness) have been proposed to describe the gouge properties. Other authors study the gouge development during the shear fracture formation of initially intact rock specimens [e.g., *Menendez et al.*, 1996; *Mair et al.*, 2000; *Wibberley et al.*, 2000].

[9] In this paper we present a study of both gouge and fracture properties of shear fractures resulting from triaxial compression tests. We present the mechanical behavior of the samples, the microstructures of the shear bands, and statistical properties of both the fracture surface roughness and of gouge granulometry. We address the influence of the confining pressure (normal stress) and of the shear displacement on both the roughness and the gouge properties.

2. Experiments

2.1. Rock Characteristics

[10] Triaxial compression tests were performed on Sidobre granite. This rock contains 71% feldspar, 24.5% quartz, 4% mica, and 0.5% chlorite. The density is 2.65 and the continuity index (sonic velocity measured on the sample divided by the theoretical value for the intact rock) is 97%. The sound velocity is 4800 m/s. The mean uniaxial compressive strength is 160 MPa, the Young modulus 60 GPa and the Poisson ratio 0.24. The diameter and length of the samples are 40 and 100 mm, respectively.

2.2. Deformation Mode

[11] The experiments consisted of deforming Sidobre granite samples under triaxial compression conditions, with confining pressure ranging from 20 to 80 MPa. The samples were subjected to axial deformation at a constant piston displacement rate until macrofailure occurred. For a first test series (gsd30), the loading was stopped immediately after the onset of the macrorupture. In the second test series (gsd40), samples underwent an additional shear loading up to a total piston displacement of 3.5 mm. The corresponding displacement along the rupture surface was estimated to ~2 mm, taking into account the shortening of the sample after the failure and the angle between the rupture surface and the core axis (near 30°).

[12] A hydraulical press of 3000 kN capacity has been used. The confining pressure was applied by means of a triaxial cell. The stiffness of the complete loading system (press, piston, sample support) is 1×10^9 N/m. The axial displacement of the platens was measured by a LVDT sensor. The sample strain was deduced from the displacement, taking into account the stiffness of the loading system (shortening of the piston) and the length of the sample. The vertical displacement rate was from 1 to 2 μm/s according to the test. In order to quantify the cracks creation and propagation during the deformation, an acoustic emission (AE) transducer was applied on the outside of the cell piston which was used as a waveguide. The AE activity quantification were done by calculating the cumulative energy of digitalized signals. The AE recording were performed on an AE system. The AE recording rate can reach hundreds of events per second when activity is very high (near the sample failure). Stress, strain and AE activity are sampled every second. This sampling rate is generally sufficient during all the test except for the macrofailure which is near instantaneous. More details on the AE system and the loading system features are given by *Amitrano and Hantz* [1998] and *Amitrano* [1999].

3. Experimental Results

3.1. Mechanical Behavior

[13] Figure 1 shows a typical mechanical behavior observed during triaxial compression. The mechanical behavior

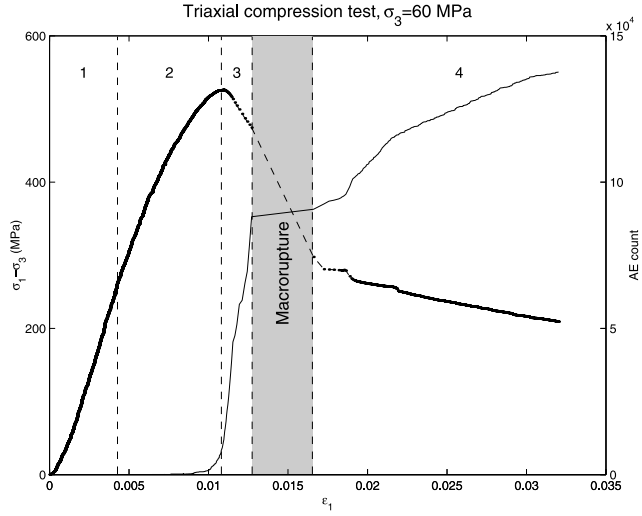

Figure 1. Typical mechanical behavior observed for the triaxial compression test gds42 at σ_3 = 60 MPa. σ_1 is the longitudinal compressive stress, σ_3 is the confining pressure, ϵ_1 the longitudinal strain. $\sigma_1 - \sigma_3$ (dotted line) and AE counts (solid line) are plotted as functions of ϵ_1. Stage 1 corresponds to the initial linear behavior, stage 2 corresponds to the nonlinear prepeak behavior, stage 3 corresponds to the postpeak behavior which leads to the macrorupture (shaded area), and stage 4 corresponds to the shearing along the macrorupture surface.

can be divided into four different stages regarding to the stress-strain curve and acoustic activity (slope of the AE counting-strain curve).

[14] During stage 1, a linear behavior with very low acoustic activity is observed. The material behavior is considered to be fully elastic with no crack propagation.

[15] Stage 2 corresponds to a nonlinear behavior before the peak stage and appears to start with the onset of the acoustic activity. Acoustic activity continuously increases and reaches its maximum as the stress peak is reached. The beginning of this stage is classically associated to the initiation of dilatancy which corresponds to the opening of cracks parallel to σ_1 [*Jaeger and Cook*, 1979; *Scholz*, 1990; *Reches and Lockner*, 1994]. AE source location reveals that, at this stage, the damage process, i.e., cracks propagation, is distributed over the whole sample in a diffuse mode [*Lockner and Byerlee*, 1991].

[16] Stage 3 corresponds to the post peak stage. The macroscopic deviatoric stress $\sigma_1 - \sigma_3$ decreases contemporary to an intense acoustic activity. During this stage, the damage localization process occurs and leads to the nucleation of a macroscopic discontinuity that results from the coalescence of microcracks [*Jaeger and Cook*, 1979; *Lockner and Byerlee*, 1991; *Reches and Lockner*, 1994]. This stage ends with the macrofailure of the sample associated to a stress release during unstable deformation. Elastic energy release from the loading press controls the mechanical path during this stage. The macrofailure is near instantaneous. The apparent linear behavior of both stress and AE during the macrofailure is due to the lack of sampling points.

[17] Stage 4 is a shearing stage during which the deformation of the sample is localized along the macrofailure surface. The deviatoric stress $\sigma_1 - \sigma_3$ decreases during shear and shows a decrease of the shear strength angle.

3.2. Influence of Confining Pressure on the Mechanical Behavior

[18] Figure 2 displays deviatoric stress, $\sigma_1 - \sigma_3$, versus axial strain, ϵ_1, for both sets of tests, either stopped or continued after the macrofailure. The mechanical behavior is clearly pressure dependent, especially the peak stress and the post failure residual shear stress. In order to highlight the influence of the confining pressure on the behavior, Figure 3 displays $\sigma_1 - \sigma_3$ at peak stress and during shear, as a function of the confining pressure, σ_3. The linear trend observed for the peak stress indicates the rock strength can be adequately fitted by a Mohr-Coulomb rupture criterion [*Jaeger and Cook*, 1979]:

$$\frac{\sigma_1 - \sigma_3}{2} = \frac{\sigma_1 + \sigma_3}{2} \sin\phi^i + S_0^i \cos\phi^i, \tag{1}$$

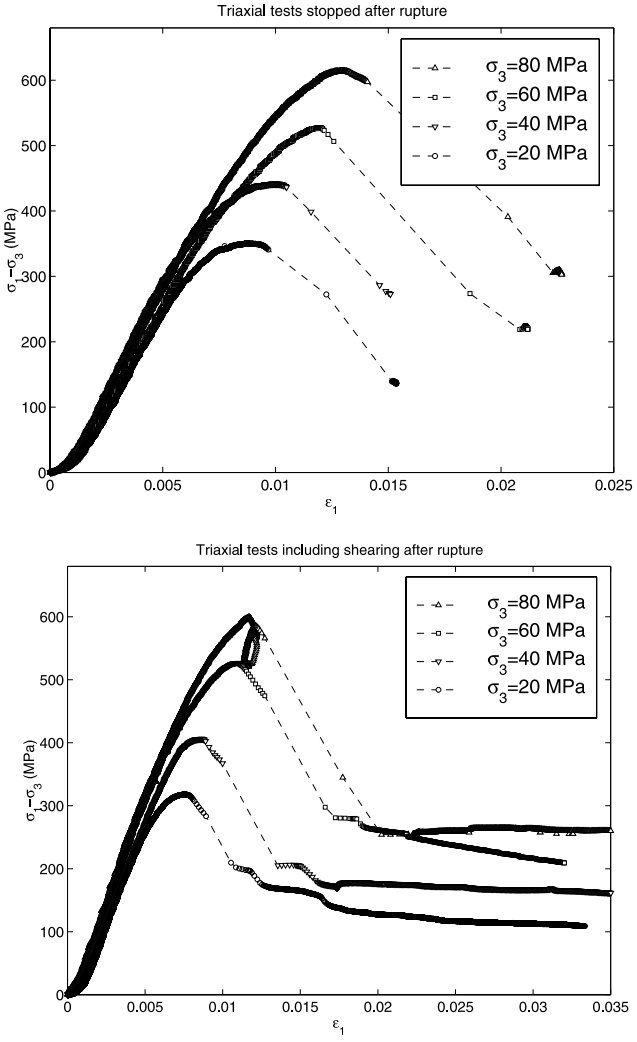

Figure 2. Mechanical behavior observed during triaxial compression tests (top) stopped and (bottom) continued after the macrorupture for confining pressures ranging from 20 to 80 MPa. σ_1 is the axial stress, σ_3 is the confining pressure, and ϵ_1 is the axial strain.

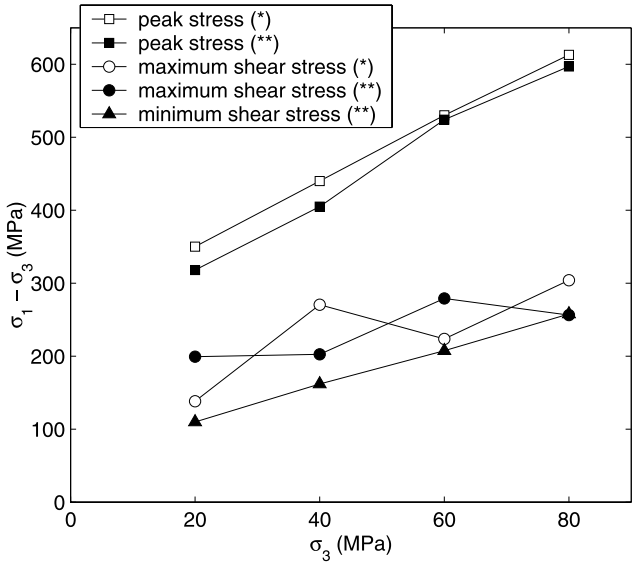

Figure 3. Differential stress, $\sigma_1 - \sigma_3$, as a function of the confining pressure, σ_3, at the peak stress and during the stages shown in Figure 1. Asterisk denotes that the tests stopped after the macrorupture, and double asterisks denote that the tests continued after the macrorupture. Maximum shear stresses are those measured directly after the macrorupture. Minimum shear stresses are those measured at the end of the shearing stage.

where ϕ^i is the internal friction angle and S_0^i is the internal cohesion.

[19] Figure 3 also indicates that the shear strength of the rupture surface obeys the classical linear friction criterion for rocks [*Jaeger and Cook*, 1979]:

$$\tau = \tan\phi\sigma + S_0, \tag{2}$$

where ϕ is the friction angle and S_0 is the cohesion.

[20] Despite the similarity between terms and denomination, equations (1) and (2) reflect two different phenomena (see *Savage et al.* [1996] for a discussion). On the one hand, the Mohr-Coulomb criterion describes the strength of a supposed continuous material in which the rupture propagates. ϕ^i refers to the pressure dependence of the strength and S_0^i to the cohesion strength of the material. On the other hand, the friction criterion describes the strength of a sheared surface. In this case, ϕ really corresponds to the frictional strength and S_0 to the apparent cohesion resulting from the imbrication of the surface at high normal stress. Estimates of these parameters are given in Table 1. The internal friction angle ϕ^i was estimated to be 55° ± 2° and the internal cohesion 37 MPa. These are typical values for a granite.

[21] For the friction criterion, no significant difference was found between the frictional angles calculated for maximum and minimum shear strengths. Both angles were estimated to be 46° ± 2°. On the contrary, we found a difference on the apparent cohesion S_0 which was 20 MPa for the maximum strength and 13 MPa for the minimum strength. The decrease of strength which occurs during shear deformation (see Figure 2) appears to be related to a decrease of the apparent cohesion and not to the decrease of the friction angle.

4. Microstructures in the Shear Bands

[22] This section describes the local mechanisms of deformation observed in the shear bands from petrographic thin sections observed under optical microscope. Complementary tests have been performed on specimens which were dedicated to the microstructure observations (three tests at respectively σ_3 = 20, 40 and 80 MPa). After completion of the tests, the samples were carefully removed from the triaxial cell and kept within their jackets to avoid damage before structural analysis. The specimens were impregnated in order to preserve their microstructure and especially to highlight fractured zones. We used a lowviscosity epoxy blue resin. The impregnation was performed under vacuum with a resin heated at approximately 50° to increase its fluidity. Because of the vacuum and the low viscosity of the resin, the impregnation was effective into the entire rupture zone for each sample. This has been verified by microscopic observations. Petrographic thin sections were cut parallel and perpendicular to σ_1. Thin section dimensions were 40 × 80 mm for the core axis parallel ones and 40 × 40 mm for the perpendicular ones.

[23] We have observed that different domains can be distinguished according to the damage level although these domains do not generally have sharp boundaries. Each domain is characterized by specific microstructures: mode I and II cracks and, gouge. A transition zone exists as shown in Figure 4 from a plane perpendicular to σ_1 (σ_3 = 40 MPa). From the left to the right, one may first observe a highly fractured and disordered material, i.e., the gouge (or cataclastic material). Only the largest grains are visible. The granular material becomes progressively ordered and the grains set appears to be more and more imbricated and tighter packed. On the right-hand side of Figure 4, the material is fractured but no grain is clearly separated. The limit between the gouge and the cracked material is not distinct but rather continuous. Accordingly, it has to be defined as a transition zone. Hence the definition of a rupture surface separating the gouge zone from the consolidated cracked zone is not simple. In Figure 4 we propose a possible extension of the transition zone. Note that the thickness of this transition zone ranges from zero (on the lower part of the photograph) to 1 mm (on the upper part of Figure 4).

4.1. En Echelon Fractures: Mode I

[24] Figure 5 shows typical mode I cracks (σ_3 = 40 MPa). Their orientation is parallel to the major compressive stress,

Table 1. Strength Parameters for Failure and Friction Criteria, Respectively[a]

Failure Criterion	ϕ_i, deg	S_{0i}, MPa
	55 ± 2	37 ± 1
Friction Criterion	ϕ, deg	S_0, MPa
Maximal shear strength	46 ± 2	20 ± 2
Minimal shear strength	46 ± 2	13 ± 1

[a]Where ϕ_i is the internal friction angle, S_{0i} is the internal cohesion, ϕ the frictional angle, and S_0 is the apparent cohesion.

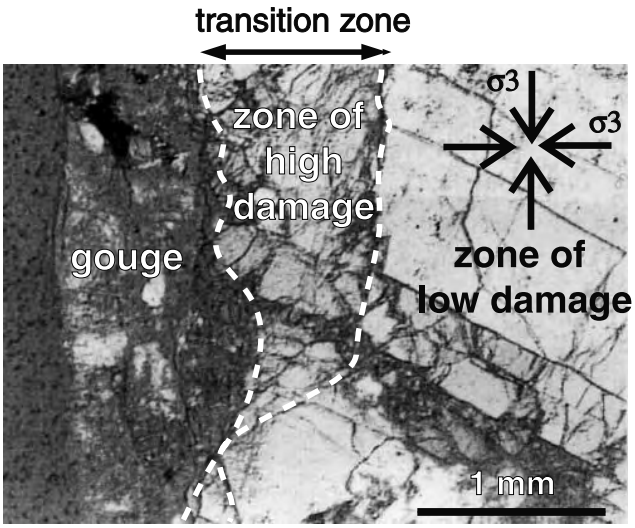

Figure 4. Thin section optical photomicrograph showing the transition between gouge, cracks, and undamaged material (plane-polarized light). The thin section cut is perpendicular to σ_1. σ_3 = 40 MPa, ϵ_1 = 0.045.

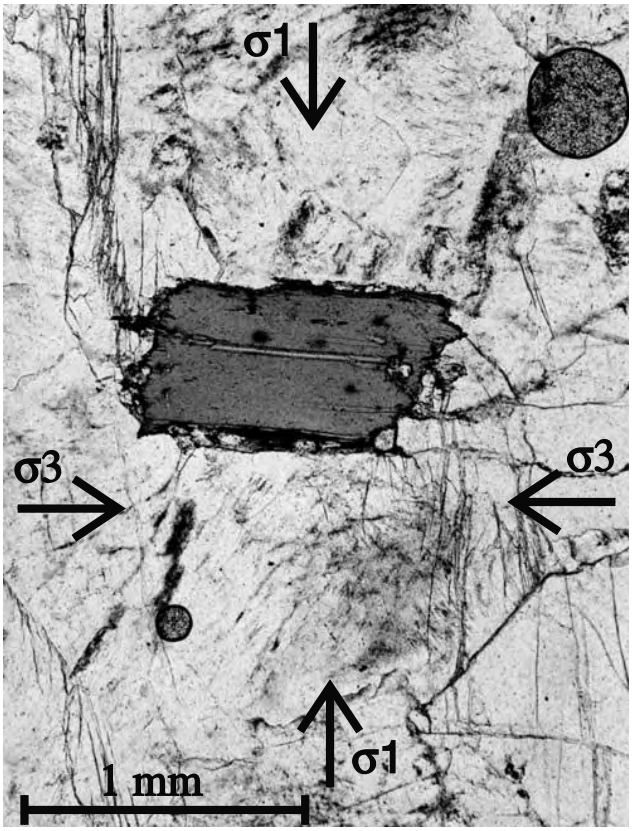

Figure 5. Thin section optical photomicrograph showing typical en echelon mode I cracks (plane-polarized light). Here the coalescence is induced by the biotite structure and the grain boundary. σ_1 and σ_3 directions are given. σ_3 = 40 MPa, ϵ_1 = 0.045.

σ_1. The crack thickness (opening) is less than 1 μm. Crack length reaches few millimeters. Coalescence of mode I cracks exists because of the very short distance between cracks, because of the geometry of the grain boundaries, due to the presence of weak planes within grains. Figure 5 shows how a biotite grain is crossed by an horizontal intergranular crack that connects two vertical cracks. This configuration is a typical en echelon crack. Such a crack pattern is observed in the whole sample: both in the shear band and far from it in the bulk sample.

4.2. Evidence of Local Mode II

[25] Clear evidence of a local mode II is visible in Figure 6 which shows the offset of a biotite mineral (σ_3 = 80 MPa). The orientation is approximately 30° with respect to σ_1 and corresponds to the orientation of the macrorupture surface. The shear displacement was estimated to be of the order of 1 mm. It is comparable to the macroscopic shear displacement of the macrorupture surface which is 2 mm for this test. This crack pattern is exclusively observed within the shear band. No similar pattern has been observed in the bulk sample.

[26] Other configurations lead to local mode II displacement due to grain rotation. An example is given in Figure 7 (σ_3 = 40 MPa). The macroscopic shearing displacement involves "block" rotation and shear displacement (at lower scale) along cracks that separate the "blocks". This can be compared to a Riedel fault as observed in geological shearing context. These "secondary" cracks have probably been created in tension mode (mode I) and then reloaded in shearing mode (mode II). Here a marker allows an estimate of the shear displacement: 0.2 mm. This deformation mode is observed exclusively within the transition zone.

4.3. Cataclastic Flow

[27] Evidence of cataclastic flow is observed within the highly comminuted zones, i.e., gouge zone as shown in

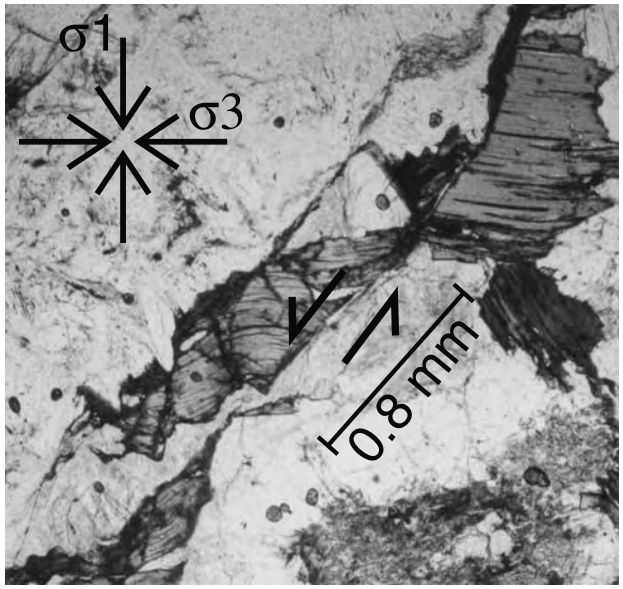

Figure 6. Thin section optical photomicrograph showing mode II cracks(cross-polarized light). The estimated tangential displacement is 0.8 mm. σ_1 and σ_3 directions are given. σ_3 = 80 MPa, ϵ_1 = 0.053.

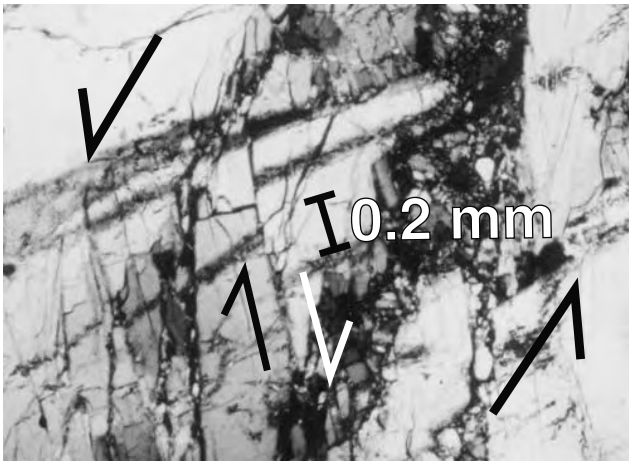

Figure 7. Thin section optical photomicrograph showing associated shearing displacements within the fractured zone (plane-polarized light). The macroscopic shear displacement involves block rotation and therefore shear at a lower scale. σ_3 = 40 MPa, ϵ_1 = 0.045.

Figure 8 (σ_3 = 80 MPa). The deformation mechanisms involve both grain rotation and grain fracturing. The latter process is shown by the strongly deformed biotite on the low-right border of the gouge layer. The offset is close to 1 mm. The thickness of the gouge zone observed in different thin sections ranges typically from 0.2 to 1 mm. These observations are comparable to those recently obtained on sandstone by *Wibberley et al.* [2000], for tests stopped after the failure, and the ones obtained by *Mair et al.* [2000, 2002], for tests including and additional shear stage. Within the gouge, more localized deformation modes appear as shown in Figure 9. One may observe shear bands, characterized by elongated zones of low diameter grains, in which the grain fracturing process occurs preferentially. The thickness of these shearing bands is 0.1 mm which is significantly smaller than the gouge thickness of 1 mm. It has been observed in previous works [*Menendez et al.*, 1996; *Mair et al.*, 2002; *Besuelle*, 2001] that shear band localization within the gouge are more developed for high normal stress than for low normal stress. We did not observe a similar effect of the confining pressure. We did neither observed any effect of the confining pressure on the gouge thickness.

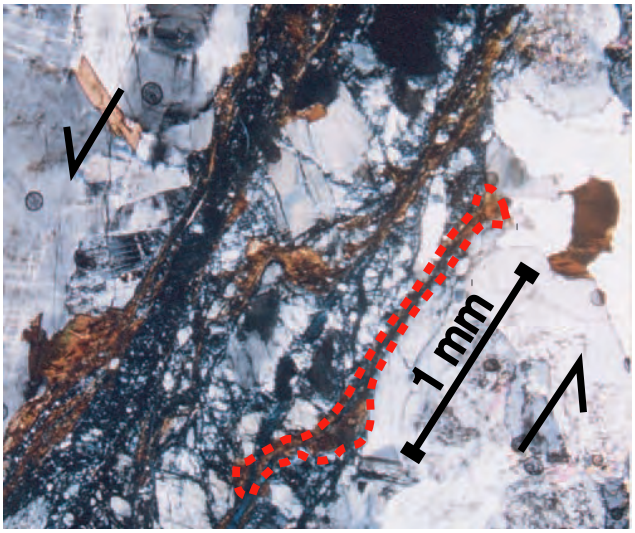

Figure 8. Thin section optical photomicrograph showing cataclastic flow within the shear zone (cross-polarized light). The dotted line labels an highly deformed biotite which allows to estimate the tangential displacement to 1 mm. The vertical direction is parallel to σ_1 and the horizontal one is parallel to σ_3. σ_3 = 80 MPa, ϵ_1 = 0.053.

5. Fracture Surface Roughness

5.1. Measurements

[28] We focus here on the description of the fracture surfaces obtained after completion of the mechanical tests. The fracture surface is the interface after opening the sample. Accordingly it corresponds to the weaker surface in the material and typically passes through the highly damaged material (i.e., transition zone) created during the compression fracture test as shown in Figure 4. After opening, unconsolidated material, i.e., gouge powder, is

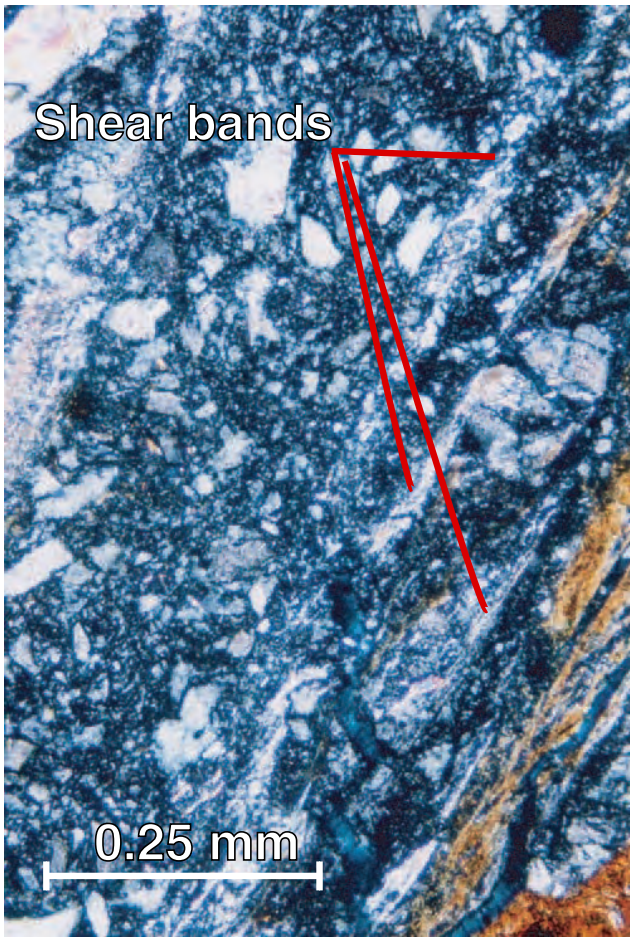

Figure 9. Thin section optical photomicrograph showing cataclastic flow of the gouge that involves shear band localization (cross-polarized light). σ_1 and σ_3 are parallel to vertical and horizontal directions, respectively. σ_3 = 80 MPa, ϵ_1 = 0.053.

Table 2. Description of the Fracture Roughness Data[a]

Sample Label	Confining Pressure, Mpa	Shearing	Final Axial Strain	Orientation	Profiles	Points per Profile	Δx, μm	Δy, μm
gsd31	20	−	0.015	parallel	11	2050	20	1000
gsd31	20	−	0.015	perpendicular	11	1030	24.5	1000
gsd33	60	−	0.021	parallel	11	2050	20	1000
gsd34	80	−	0.022	parallel	10	2050	20	1000
gsd34	80	−	0.022	perpendicular	11	1030	24.5	1000
gsd41	20	+	0.033	parallel	11	2050	20	1000
gsd42	40	+	0.035	parallel	11	2050	20	1000
gsd43	60	+	0.032	parallel	11	2050	20	1000
gsd43	60	+	0.032	perpendicular	11	1030	24.5	1000
gsd44	80	+	0.035	parallel	11	2050	20	1000
gsd44	80	+	0.035	perpendicular	11	1030	24.5	1000

[a]Either an absence (−) of shearing after the macrofailure or the presence (+) of shearing after the macrofracture is indicated. When the fracture surface extends completely through the length and the width of sample, a roughness measurement of 10 or 11 profiles has been performed along two perpendicular directions: one along the slip and one perpendicular to it. Δx and Δy are the step size along the x direction (profile direction) and y direction (distance between profiles), respectively. Profile sampling density was adjusted to explore the longest part along the specific direction of the sample and to be compatible with the profiler resolution.

blown out with an air flow and a brush. The topography that is left is partly sampled with a mechanical profiler [*Lopez and Schmittbuhl*, 1998]. The profiler has a resolution of 5 μm for horizontal positioning and 3 μm along the vertical axis. In most cases we sampled the surfaces only parallel to the presumed slip direction. Indeed, we measured 11 parallel profiles along each analyzed surface. Table 2 describes the roughness measurements that were performed. However, when surfaces were sufficiently extended (4.5 mm × 3 cm), they were measured along two perpendicular directions (parallel and perpendicular to the slip direction). The number of sample points per profile has been adjusted to obtain the highest density of points: 2050 points along the slip direction and 1030 points perpendicular to the slip direction. Parallel profiles are considered to be sufficiently separated (1 mm) to be statistically independent. Except for one surface, sampling for roughness measurements along the slip direction consists of 22,550 points and of 11,330 points for sampling perpendicular to the slip direction. The total set of data corresponds to 201,120 sampling points.

[29] Two representative profiles are shown in Figure 10. They come from the test gsd34 (80 MPa of confining pressure, without imposed shear). Figure 10a represents a profile along the slip direction, and Figure 10b represents a profile perpendicular to it.

5.2. Spatial Correlations and Self-Affine Properties

[30] Fracture surfaces have been largely studied [*Mandelbrot et al.*, 1984; *Maloy et al.*, 1992; *Cox and Wang*, 1993; *Power et al.*, 1987; *Power and Durham*, 1997]. Successful quantitative descriptions have been obtained on the basis of scaling invariance, more precisely self-affine properties [*Schmittbuhl et al.*, 1993, 1995b; *Bouchaud*, 1997; *Lopez and Schmittbuhl*, 1998]. If $h(x,y)$ is the topography of the fracture surface where x and y are two perpendicular directions along the mean fracture plane, an isotropic self-affine surface shows statistically the following invariance [*Feder*, 1988]:

$$h(\lambda x, \lambda y) = \lambda^{\zeta} h(x,y), \tag{3}$$

where λ is a scaling parameter and ζ the roughness exponent or Hurst exponent. Surprisingly, the roughness exponent is found for numerous fracture surfaces to be close to 0.80 [*Bouchaud*, 1997]. Such a property has been proposed as a possible universal property of fracture surfaces by [*Bouchaud et al.*, 1990]. Recently, a roughness exponent significantly different: $\zeta \approx 0.5$ has been obtained

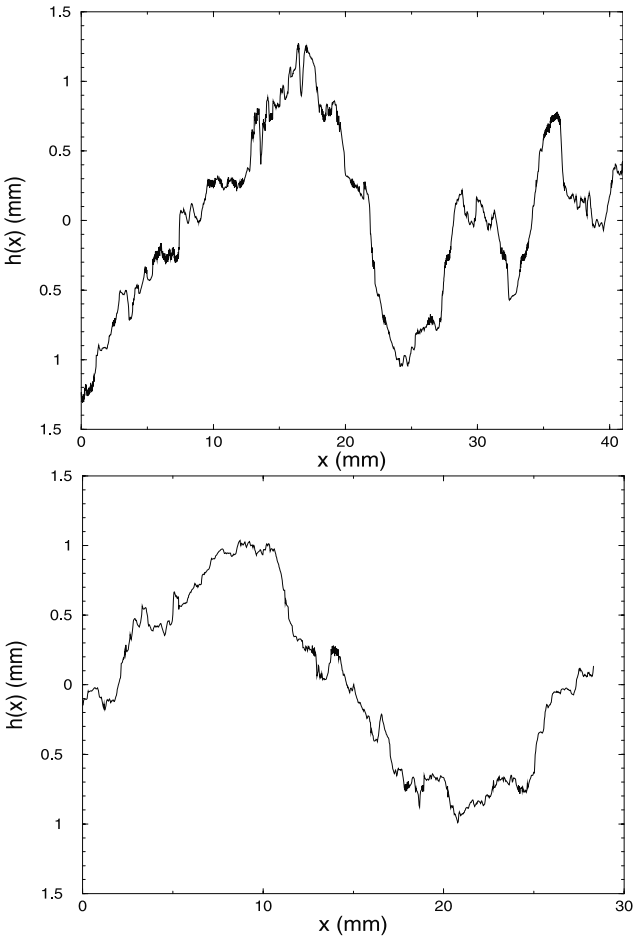

Figure 10. (top) One profile from the fracture surface gsd34 (80 MPa of confining pressure) along the slip direction. (bottom) One profile from the same surface but in the perpendicular direction. Regions that appear as a thick line correspond to highly damaged zones.

for sandstone [*Boffa et al.*, 1998]. The existence of two roughness exponents, one for small scales ($\zeta = 0.5$) and one for large scales ($\zeta = 0.8$) has also been proposed by [*Bouchaud*, 1997].

[31] Links between isotropic fractals and self-affine fractals have been studied [*Feder*, 1988; *Falconer*, 1990; *Yang and Lo*, 1997]. For instance, the link between the fractal dimension D and the roughness exponent ζ for profiles is $D = 2 - \zeta$. One has to note that the roughness exponent is smaller than one, meaning that the large-scale slope $s = \Delta h/\Delta L \propto \Delta L^{1-\zeta}$ of a profile reaches zero for large scales. Accordingly, fracture surfaces appear flat at large scales.

5.3. Self-Affine Analyses

[32] Several tools exist to analyze self-affine properties of rough surfaces. We used five independent techniques among them: The RMS, the maximum-minimum difference, the return probability, the Fourier spectrum, and the Wavelet spectrum [*Falconer*, 1990; *Schmittbuhl et al.*, 1995a; *Simonsen et al.*, 1998]. Each of these methods is supposed to show a power law behavior with an exponent directly related to the roughness exponent ζ. In more detail, the RMS technique measures the root mean square of the profile $h(x)$ for different window sizes d. For each window size the RMS $w_2(d)$ is averaged over the different positions of the window along the profile. The expected behavior for a self-affine profile with a roughness exponent ζ is $w_2(d) \propto d^{\zeta}$. The maximum-minimum difference (MMD) technique consists of searching for the difference between the maximum and minimum height $w_\infty(d)$ for a size of the window d. For a monofractal self-affine set, the expected behavior is $w_\infty(d) \propto d^{\zeta}$. The main difference between $w_2(d)$ and $w_\infty(d)$ is that the former is related to the second order moment of the height distribution whereas w_∞ is related to the infinite moment of the distribution. Differences between both estimates are related to a multifractal behavior. The return probability $P(d_0)$ is computed from the distribution of the cut lengths d_0, when cutting the profile with lines parallel to the average trend of the profile (i.e., horizontal lines). The probability distribution for a self-affine fractal is $P(d_0) \propto {d_0}^{2-\zeta}$. To increase the reliability of this technique, logarithmic binning is often used, in which case, the return probability behaves as: $P_{lb}(d_0) \propto {d_0}^{1-\zeta}$ [*Schmittbuhl et al.*, 1995a]. The Fourier spectrum is the spectrum of the modulus square of the Fourier transform. To avoid problems from non periodic profiles, we suppress the linear trend estimated as the line from the first to the last point along each profile. For a self-affine profile, the power spectrum is supposed to behave as: $P(k) \propto k^{-1-2\zeta}$ where k is the wavelength. The last technique is more recent [*Mehrabi et al.*, 1997] and presented as the Average Wavelet Coefficient technique by [*Simonsen et al.*, 1998]. It consists of averaging the Wavelet transform $W_b(a)$ of the profile over the translation factor b for a given scale factor a. We used Daubechies wavelets [*Press et al.*, 1992]. The expected behavior for this technique is $W(a) \propto a^{\zeta+1/2}$. The latter technique has been shown to be extremely sensitive, precise and robust [*Simonsen et al.*, 1998].

5.4. Results

[33] Each of the five techniques has been applied on all data sets presented in Table 2. Figure 11 shows the analysis for each technique applied on profiles oriented along the slip direction. Plots are in log-log coordinates to emphasize a possible power law behavior illustrated by a guidance line on each graph. The five techniques show a set of curves that is very consistent with a power law behavior over at least 2 orders of magnitude. Such a behavior is the hallmark of a self-affine scaling of the fracture roughness. A second important finding from Figure 11 is that the geometrical properties of the fracture surfaces are weakly sensitive to the mechanical path. Indeed, for all techniques, all curves are close to being superimposed. This clearly shows that the fracture geometry (more specifically the spatial correlations that exist along the fracture geometry) are very robust even if the mechanical load is different: (1) the influence of the confining pressure (from 20 to 80 MPa) is weak; and (2) quasi-static or dynamical shear produces the same roughness. Indeed, surfaces from the series gsd30 tests are created after a short dynamical shear. On the contrary, tests from the series gsd40 correspond to a long slow quasi-static shear.

[34] A first estimate of the roughness exponent is obtained from the guidance line on each figure. The different methods are very consistent and show that the roughness exponent is close to 0.75 as classically obtained for fracture surfaces [*Power et al.*, 1987; *Schmittbuhl et al.*, 1995b; *Bouchaud*, 1997; *Power and Durham*, 1997]. We emphasize that the results obtained from previous studies on artificial fracture mainly concern tensile fractures. Very few analyses of the scaling properties of artificial shear fractures are reported in the literature. [*Power and Durham*, 1997] report on the power spectra of profiles from a shear fracture in Westerly Granite. They obtained very similar results for the roughness exponent from two triaxial tests: a fast one and a slow one. The fact that the roughness of tensile and shear fractures is very similar, is not obvious since the fracture processes are different. Shear cracks are not surface free processes and involve significantly higher energy release rates [*Atkinson*, 1991]. However some similarities in the elastic influences on the stress field along the crack tip can be obtained theoretically [*Gao and Rice*, 1986; *Gao et al.*, 1991; *Atkinson*, 1991; *Schmittbuhl et al.*, 2002].

[35] A more quantitative comparison between methods and mechanical paths is possible by comparing the roughness exponent estimates for each profile set as listed in Table 3. Systematic biases exist for each technique. They are precisely quantified by *Schmittbuhl et al.* [1995a] and *Simonsen et al.* [1998]. The RMS technique and to a lesser extent the MMD technique have been shown to underestimate roughness exponent systematically when measuring high roughness exponents. Accordingly, estimates reported for W_2 in Table 3 are somehow systematically lower than the others. *Schmittbuhl et al.* [1995a] predict that the correction should be close to +0.08. The first return probability technique plotted in Figure 11c, is very sensitive to the fitting range since there exists a significant cutoff for large return distances d_0, because of the limited sampling. The Fourier spectrum estimate was proposed by [*Schmittbuhl et al.*, 1995a] as the most reliable. However the recent wavelet technique (AWC) proposed by *Simonsen et al.* [1998] is even more precise and less sensitive to local artifacts, like profiler errors, or large-scale artifacts like nonperiodicity of the profiles. In the application of our results, we rely mostly on the two latter techniques.

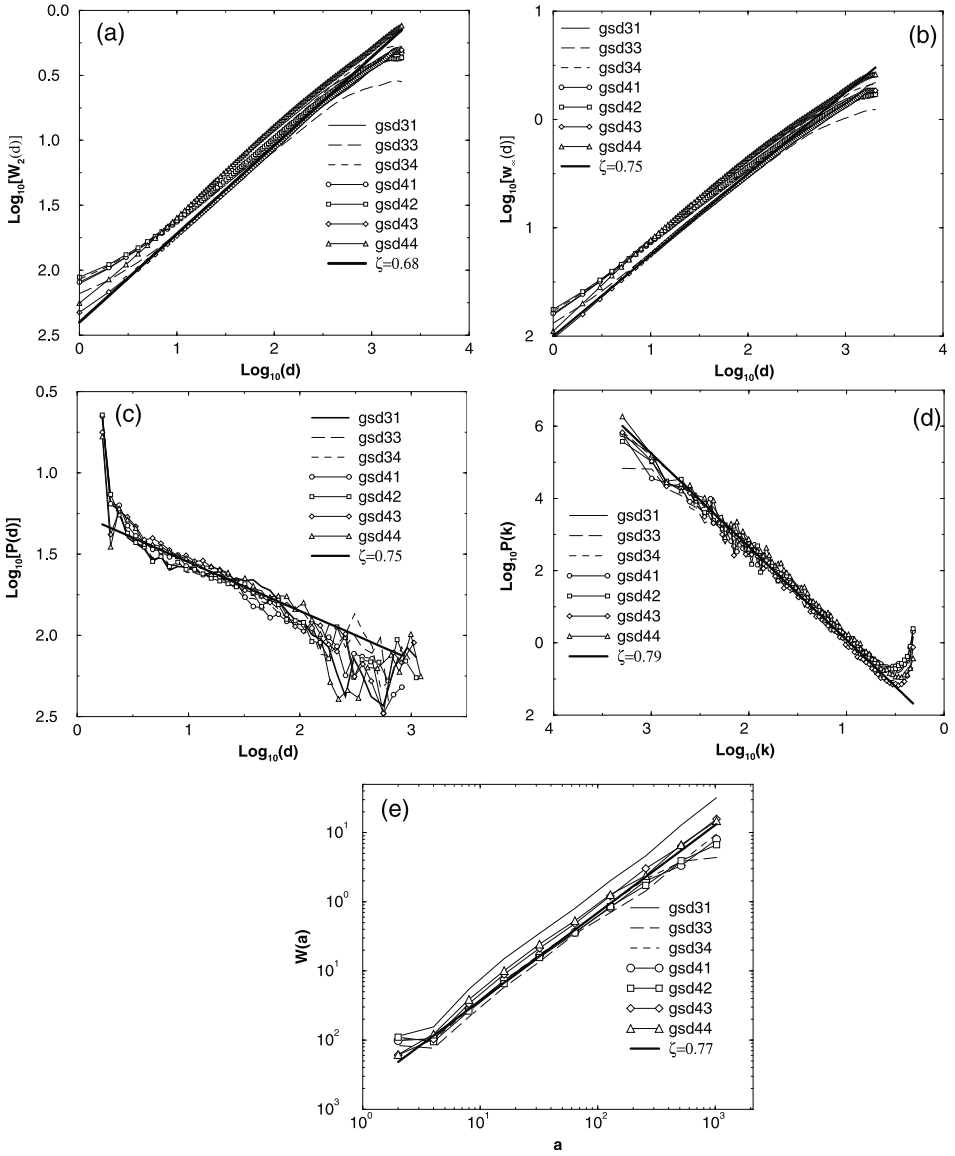

Figure 11. Roughness scaling analysis from five independent techniques: (a) RMS, (b) MMD, (c) first return probability with logarithmic binning, (d) Fourier spectrum, and (e) average wavelet coefficient. Curves are fitted using power law. A sample power law with a prescribed roughness exponent is shown on plot for eye guidance. Only data sets of profiles oriented along the slip direction are reported. Each curve is an average over the analysis of each profile of the data set. Fits are performed for each curve, and corresponding roughness exponents are listed in Table 3.

[36] When considering the measurement biases mentioned previously, estimates of the roughness exponent from the five techniques are very consistent. Subsequently, a more detailed comparison of the samples can be performed. Figure 12 shows the evolution of the roughness exponent ζ with the confining pressure using the three most reliable techniques (i.e., MMD, power spectrum and wavelet spectrum) for both series of tests and measurements along the slip direction: one stopped just after the rupture (gsd30 series) and one with a supplementary imposed slow shear (gsd40 series).

[37] As mentioned previously, sensitivity to the confining pressure during the test is weak. However when comparing evolution without and with shearing, the effect of the confining pressure can be observed: when stopped just after macrofailure, i.e., the peak stress, the roughness exponent ζ slightly decreases with confining pressure σ_3 increase. After an imposed shear, there is a significant evolution of the geometry of the surface. At low confining pressure (20–40 MPa), the roughness exponent decreases. On the contrary at higher confining pressure (60–80 MPa), the roughness exponent increases. Accordingly, there is an opposite effect of the shear on the fracture roughness when changing the confining pressure. Shear at low confining pressure tends to roughen the fracture surface. On the contrary, at high confining pressure, the slow shear process smooths the fracture surface and increases the spatial correlations along the topography of the surface.

Table 3. Estimates of the Roughness Exponent[a]

Sample	$W_2(d)$	$W_\infty(d)$	$P_{lb}(d_0)$	$P(k)$	$W(a)$
gsd31	0.66	0.74	0.79	0.75	0.77
gsd33	0.63	0.71	0.75	0.74	0.70
gsd34	0.65	0.71	0.68	0.75	0.74
gsd41	0.61	0.69	0.62	0.70	0.71
gsd42	0.63	0.70	0.72	0.71	0.71
gsd43	0.67	0.74	0.65	0.76	0.78
gsd44	0.71	0.78	0.72	0.76	0.74
Average	0.65	0.72	0.70	0.74	0.74
gsd31[b]	0.79	0.85	0.68	0.85	0.88
gsd34[b]	0.66	0.74	0.66	0.72	0.69
gsd43[b]	0.77	0.80	0.66	0.83	0.82
gsd44[b]	0.74	0.80	0.67	0.83	0.80
Average[b]	0.74	0.80	0.67	0.81	0.80

[a]For each technique, RMS $W_2(d)$, maximum-minimum difference $W_\infty(d)$, return probability $P_{lb}(d_0)$, power spectrum $P(k)$, and wavelet spectrum $W(a)$; the roughness exponent is measured from the fit of the average curve over all the profiles measured on the sample along the slip direction. Error bars for the roughness exponent estimates are 0.02.

[b]Corresponds to profiles perpendicular to the slip direction.

[38] From the measurement of the roughness along profiles perpendicular to the slip direction (i.e., samples labeled with a star in Table 3), the anisotropy of the fracture roughness can be addressed. Unfortunately, we were not able to sample all surfaces along the perpendicular direction because of the limited width of the biggest fracture surface developed in the samples. However, average estimates in Table 3 show a slightly higher exponent for profiles perpendicular to the slip direction. For instance the AWC technique ($W(a)$) indicates an average roughness exponent for profiles along the slip direction of $\zeta = 0.74$ and of $\zeta^* = 0.80$ for profiles perpendicular to the slip direction. Surfaces are rougher along the slip than perpendicular to it. Accordingly spatial correlations are on lower scales along the slip than perpendicular to it. There is a small anisotropy along the fracture surfaces that corresponds to the stria created during the shear process. This result is consistent with observations reported by *Power and Durham* [1997].

6. Gouge Particle Size Distribution

[39] This section addresses the geometric properties of the gouge material, particularly the particle size distribution, i.e., granulometry.

6.1. Grain-Size Measurement

[40] After each test, the gouge material in-filling in the rupture zone was carefully extracted for granulometry measurement. The grain-size distribution of the gouge has been measured by mean of a Laser Particle Size Analyzer (LPSA). The granular material is suspended in a solution of distilled water and introduced between a laser source and a detector. The laser beam of the LPSA is diffracted by each particle according to its curvature and its reflective index. Considering the grains as spherical and having all the same reflective index, the diffraction angle is only a function of the grain radius. Therefore diffraction data might be used to estimate the grain-size distribution. Comparisons with other granulometry measurement techniques have shown the reliability of the technique [*Mair et al.*, 2000]. Advantages of this technique are mainly the broad range of grain size that can be measured simultaneously (from 2 μm to 2 mm in diameter) and the high speed of the measurements. Disadvantages are the necessary assumptions that grains are spherical and that they have all the same reflective index. For highly angular grain these assumptions may lead to an overestimate of their size.

[41] Grain-size distributions are given as the volume histogram of 20 diameter bins that are equally log-spaced between 2 μm and 2 mm. The volume histogram is converted into the grain number distribution considering spheres of equivalent volume.

6.2. Grain-Size Distribution

[42] Figure 13 displays the density probability distribution of grain size obtained for the different confining pressures, respectively with or without shearing after the macrofailure. The linear trend of the distribution on a bilogarithmic plot, indicates that the distribution can be fitted by a power law:

$$P(D) = cD^{-e}, \tag{4}$$

where $P(D)$ is the proportion of grains of diameter D, c is a prefactor and e is the power law exponent, considered as the fractal dimension of the grain assembly.

[43] Probability density distributions are obtained by differentiating the measured cumulative distributions. Because of the logarithmic binning, the exponents for cumulative and density distribution are equal [*Lahaie*,

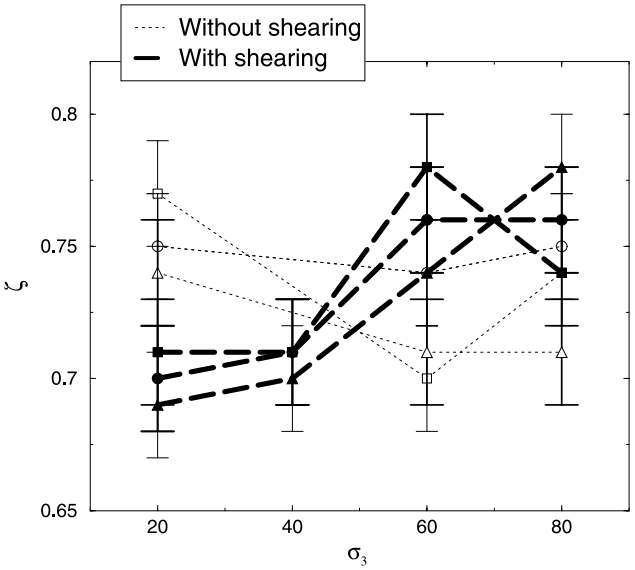

Figure 12. Influence of the confining pressure σ_3 on the roughness exponent of the fracture surfaces along the slip direction. Squares correspond to estimates using the AWC technique ($W(a)$); circles are obtained with the power spectrum method, and triangles are obtained with the maximum-minimum difference technique. When no shearing is imposed after fracture (gsd30 series), the roughness exponent slowly decreases with the confining pressure. On the contrary, when a postrupture shear is imposed (gsd40 series), the roughness exponent increases with the confining pressure.

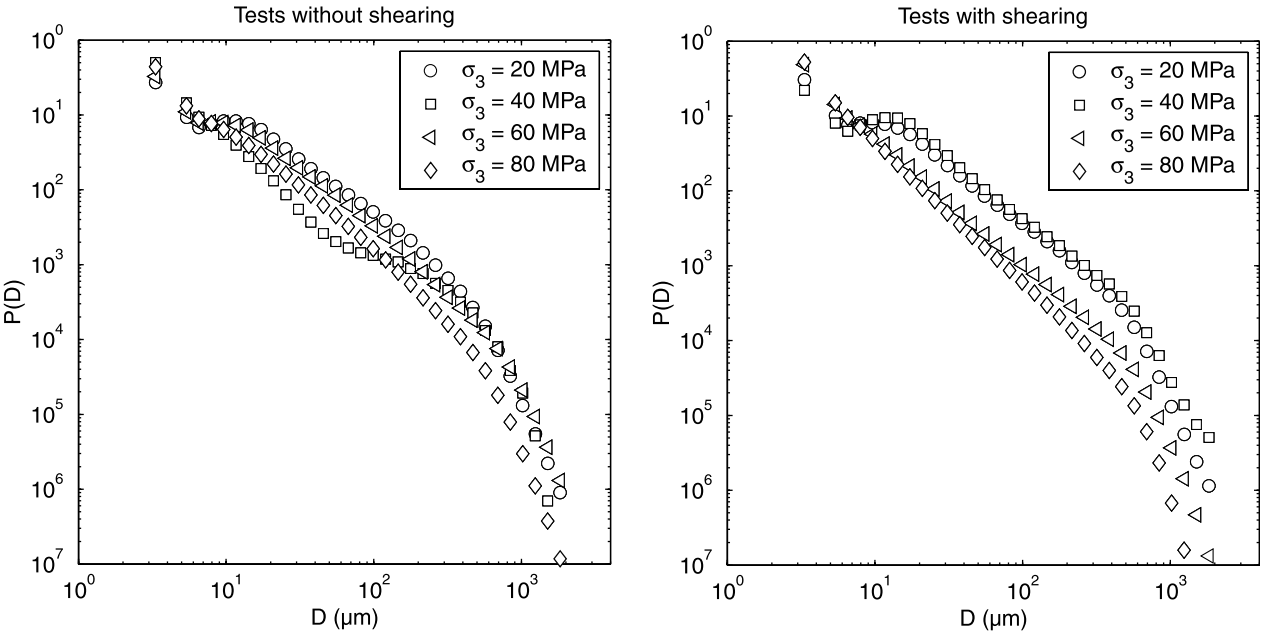

Figure 13. Density probability distribution of the grain size for tests (right) with or (left) without shearing after the macrofailure.

2000]. In order to estimate the width of the power law distribution, we used the two points slope technique. The local curve slope, s_l, is calculated between every point of the distribution ($s_l = \Delta P(D)/\Delta D$). The range over which s_l is constant gives the width of the power law behavior.

[44] A supplementary reliability check of the power law fit, is performed using a χ^2 test. We calculated the χ^2 distance between the observations and the power law fit.

$$\chi^2_{\text{dist}} = \sum_{k=1}^{r} \frac{\left(P^k_{\text{obs}} - P^k_{th}\right)^2}{P^k_{th}}, \tag{5}$$

where P^k_{obs} is the observed value for bin k, P^k_{th} is the theoretical value for bin k (given by the fitted power law), and r is the total number of bins. The χ^2_{dist} is compared to the theoretical χ^2 value for a 1% risk level and r degrees of freedom ($\chi^2_{1\%}$). If $\chi^2_{\text{dist}} < \chi^2_{1\%}$ the observed distribution is correctly fitted by a power law. On the contrary, if $\chi^2_{\text{dist}} > \chi^2_{1\%}$, the fit is rejected. In the latter case, the bin that shows the greatest deviation from the power law fit, is removed until the test becomes acceptable. The result of the power law fit is shown in Figure 14. Exponents are calculated using a 95% confidence level interval.

6.3. Effect of the Displacement and of the Confining Pressure

[45] To estimate the effect of shear displacement on particle size distribution, we compare distributions obtained from tests stopped just after the macrorupture to those obtained from tests that include a postpeak shear displacement (Figure 14). Except for σ_3 = 40 MPa, particle size distributions for tests without imposed shear are above those for tests with a shear stage. The proportion of small particles increases with the imposed postpeak shear displacement. This can be considered as a consequence of the grain fragmentation during shearing. Accordingly, the width of range of the power law behavior is larger for tests with shearing, particularly for small particles.

[46] Figure 15 displays the effect of both the confining pressure and the shearing displacement on the e exponent. Except for σ_3 = 40 MPa, the e exponent is higher for tests that include shearing than for the ones without shearing. Note that the e value which corresponds to the test performed at σ_3 = 40 MPa without shearing (see Figure 15), appears to not fit the trend. In Figures 2 and 3, one may observe that this test was stopped at an anomalously high stress value which suggests that the rupture zone was not fully developed. This might explain the high value of the e exponent. Tests stopped after the macrofailure (i.e., after the peak stress), do not reveal a clear trend of the e exponent with the confining pressure. On the contrary, the e exponent significantly increases with the confining pressure when tests include shearing after the macrofailure.

7. Discussion

[47] Qualitative observations of petrographic thin sections revealed that the rupture zone is thick because of a transition zone between the relatively intact host rock (bulk) and the gouge material. It is mainly within this transition zone that the macrorupture surface develops.

[48] In the bulk, we mainly observed mode I cracks parallel to σ_1 characterized by a very low aperture (>1 μm) compared to their length (up to several millimeters). These cracks are observed to be intergranular, intragranular, and transgranular. As generally admitted, these cracks start to propagate contemporaneously to the onset of dilatancy, before the macrorupture, and their coalescence leads to the nucleation of the macrorupture [*Brace et al.*, 1966; *Jaeger and Cook*, 1979; *Costin*, 1983; *Kranz*, 1983; *Reches and Lockner*, 1994; *Schulson et al.*, 1999].

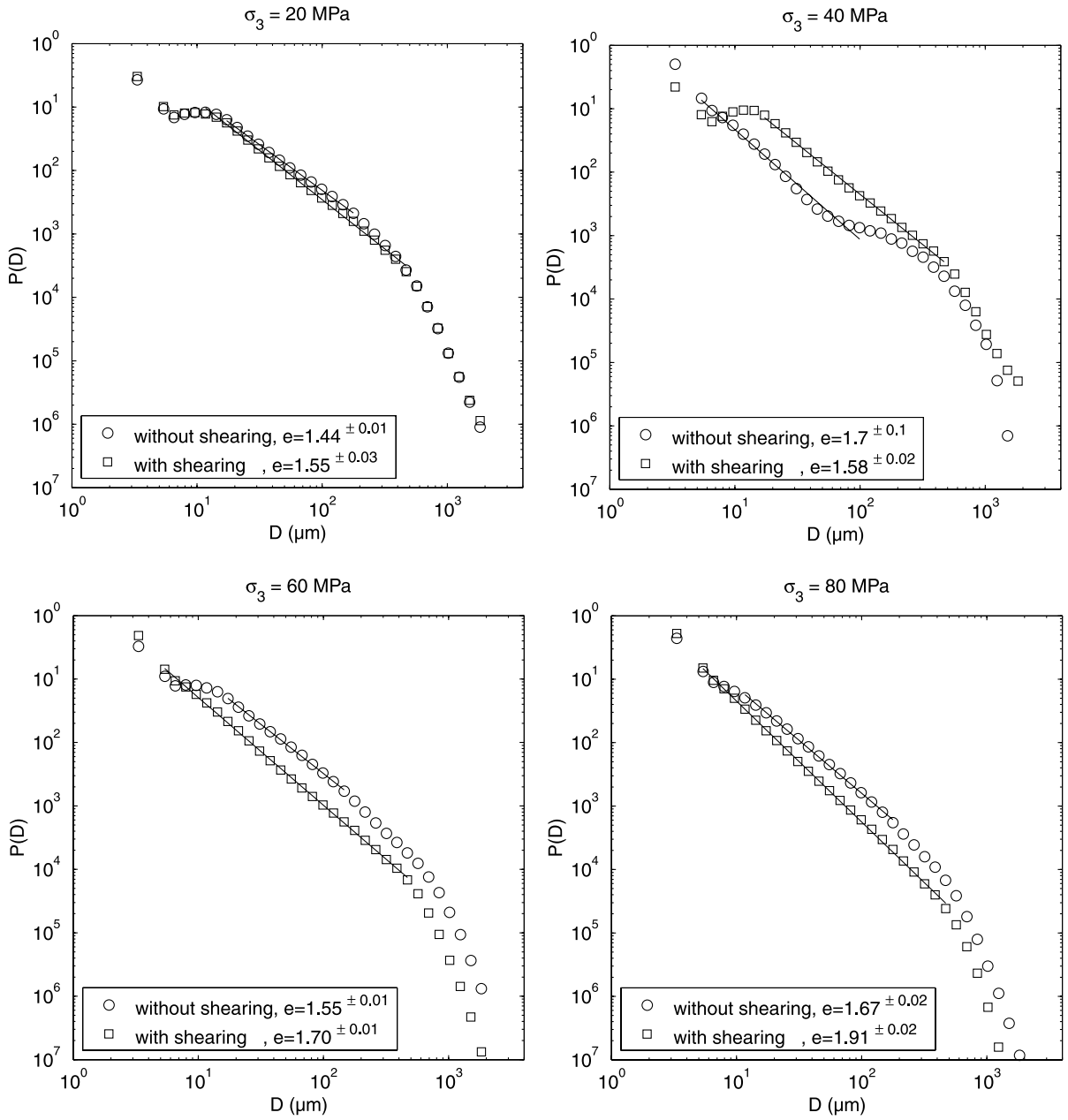

Figure 14. Probability density distributions of the grain size for tests with (square) or without (circle) shearing after the macrorupture for the different confining pressures, σ_3. Lines indicate the power law range. The e exponent is given with an estimate error for a 95% confidence level.

[49] Mode II cracks are observed exclusively within the transition zone. It is difficult to say if these cracks have been generated before or after the macrorupture. Mode II cracks are locally included into a complex deformation mode like Riedel-like fracture. Hence we distinguish two types of mode II cracks according to the magnitude of the shear displacement. First-order displacements are directly related to the shear deformation of the rupture zone (see Figure 6). Second-order displacements are related to grain rotation or Riedel-like fracture (see Figure 7). Measurements of the shear displacement on these two types of cracks have been performed. First-order displacements are estimated to be in the range 1–2 mm which is comparable to the shearing displacement of the fracture at the sample scale. The second-order shear offsets are estimated to be smaller than 0.1 mm.

[50] In the rupture zone, gouge material has been observed and indicates a cataclastic deformation mode. From our observations, the gouge thickness ranges from 0.1 to 1 mm. Within the granular material, we observed subshear band localization characterized by finer grains compared to the embedding gouge. Their thickness has been estimated to be of the order of 0.05–0.1 mm depending mainly on the gouge thickness. This is in agreement with the observations of *Mair et al.* [2000, 2002] and indicates that the fracturing process is efficient over a wide range of scales.

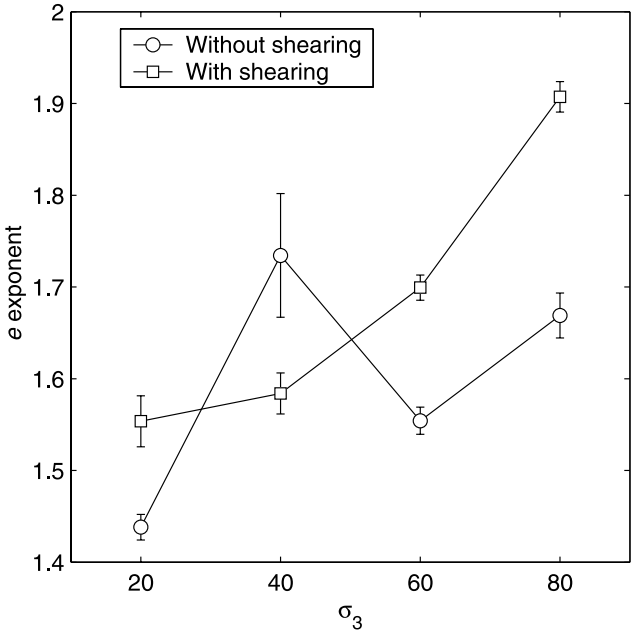

Figure 15. The *e* exponent as a function of confining pressure for tests with (squares) or without (circles) shearing after the macrofailure, respectively. The vertical bars give the estimate error for a confidence level of 95%.

[51] The power law exponent *e* of the grain-size distribution can be regarded as the relative proportion of small versus large particles (a high e exponent corresponding to a high proportion of small particles). Accordingly, two conclusions can be drawn: (1) the proportion of small particles increases during the shearing deformation; and (2) the proportion of small particles increases with the confining pressure.

[52] As addressed in recent works on sandstones, these effects could result from the gouge fracturing process which occurs during the shear deformation. For tests stopped after the end of the macrofailure phase, *Wibberley et al.* [2000] observed that the mean grain size of gouge in-filling the fracture decreases with increased normal stress. For samples deformed after the failure, *Mair et al.* [2000] observed that the number of shear bands increased with the accumulated strain. More recently, they observed that the number of shear bands increased with the confining pressure [*Mair et al.*, 2002]. As the shear bands are composed by highly comminuted material, this is in agreement with our observation of increasing proportion of small particles as the deformation progresses. These results indicates also that the comminution process becomes more efficient as the confining pressure increases.

[53] Moreover, the power law fit of the particle size distributions is possible on a broader range for tests with shear displacement. Error bars are smaller. The range increase indicates that the scaling invariance extends to a larger range of scales as the deformation increases.

[54] We observed that the fracture surface roughness displays self-affine scaling properties with a roughness exponent close to $\zeta \approx 0.80$. The roughness exponent ζ obtained for tests with or without shearing, have been compared for various confining pressures. The roughness exponent is weakly sensitive to the shear displacement and to the confining pressure. Small differences still exist. They are of two types. At low confining pressure (σ_3 = 20 and 40 MPa), ζ is lower for tests with shear displacement. On the contrary, for high confining pressure, (σ_3 = 60 and 80 MPa), ζ is higher for tests with a shearing stage. We observed a systematic increase of ζ with the confining pressure for tests with a shear stage. As ζ describes the smoothness of the surface, these results can be summarized as follows: when sheared the rupture surfaces become rougher at low confining pressure and smoother at high confining pressure.

[55] The confining pressure influence on fracture roughness may be related to the amount of sample dilation which has been shown to depend on the confining pressure [e.g., *Menendez et al.*, 1996]. Because of geometrical effects, the shearing of a rough surface induces dilatancy [*Barton and Choubey*, 1977]. At low confining pressure, the dilatancy is weakly impeded and the shearing may occurs with limited surface erosion. At high confining pressure, the dilatancy is impeded, which enhances the surface erosion; hence the reduced roughness allows deformation with reduced dilatancy. For our tests, we do not have volumetric measurement that could reveal difference in sample dilation related to the confining pressure.

[56] This explanation could be relevant for the smoothing we observed at high confining pressure but not for the roughening at low confining pressure. For the latter, we propose the following interpretation. We suggest that a gouge roughness coupling process exists and that it depends on the confining pressure. For low confining pressure σ_3, the decrease of ζ indicates that the fracture surface becomes rougher as the shearing progress. This roughening comes from an evolution of the rupture surface into the transition zone. On the contrary, for high confining pressures, the increase of ζ indicates that the fracture surface becomes smoother as the shearing progresses. This smoothing leads to a morphological simplification of the transition zone.

[57] This interpretation is in agreement with results of *Wibberley et al.* [2000], who observed that tensile microcracks were releasing material from the intact wall rocks and this material was being incorporated into the microfault as shearing occurred. We observed similar features for our experiments as shown in Figure 16. This process is particularly well highlighted by rotating fragments at the border of the gouge zone.

[58] We propose a simple model to illustrate a possible coupling between gouge and fracture roughness. Our model is purely geometrical one. We assume that a first surface with a roughness exponent ζ_1 is sheared and a new surface is generated. That new surface is supposed to be correctly described by a new roughness exponent ζ_2. Because we consider a quasi-static evolution of the fracture surfaces, magnitude (i.e., RMS) of the surfaces is conserved. The purpose of this model is to compare the volume of material that is extracted when the fracture surface is transformed. To make it even more simple, we consider a two dimensional model (i.e., surfaces are reduced to profiles). Profiles of 65,536 points are generated using a Fourier algorithm. We measure the areas of

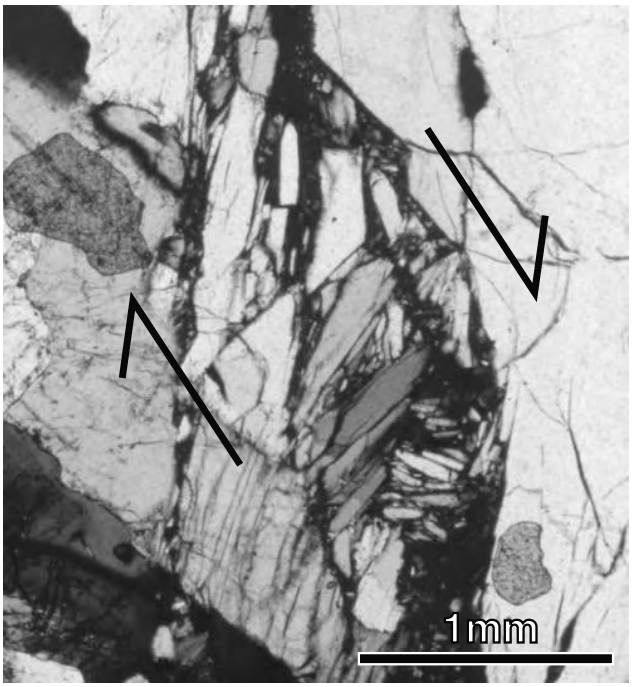

Figure 16. Thin section optical photomicrograph (cross-polarized light) showing the process of erosion of the transition zone during the shearing. Particles are released from the transition zone and incorporated in the gouge material. σ_1 and σ_3 are parallel to vertical and horizontal directions, respectively. σ_3 = 40 MPa, ϵ_1 = 0.045.

material that would disappear because of the transformation. These areas are measured by a effective diameter that is the square root of the area. In Figure 17, we show the histograms of the particle size for different roughness exponents ζ_2. The roughness exponent ζ_1 is chosen as the measured roughness exponent just after failure: ζ_1 = 0.8. We see from Figure 17 that the distribution is a power law distribution for large particles with a slope that increases with the final exponent ζ_2. When there is no evolution of the roughness exponent ($\zeta_1 = \zeta_2$), particles are created since the final surface is statistically independent of the initial surface but the distribution is flat. If the final roughness exponent is significantly decreased, the created particles are much finer and the slope of the distribution is very negative. However, for the change of roughness exponent that is observed experimentally, the particle size distribution is close to flat. As a consequence, this process does not account for the significant increase of the exponent *e* that is observed for high confining pressure. However, it might explain why the particle size distribution is, for low confining pressure, significantly smaller than for fragmentation distribution.

8. Conclusion

[59] Triaxial compression tests on Sidobre granite have been performed at confining pressure ranging from 20 to 80 MPa. We have compared tests stopped immediately after the macrorupture and tests that include a supplementary shearing stage. Direct observations from thin sections of the shear zone have been performed for various confining pressures. We observed that different deformation modes were acting during the shearing, i.e., mode I and mode II cracks, cataclastic flow, subshear band localization.

[60] The transition between the intact material (that included mode I cracks) and the gouge material is not sharp and the limit between them is difficult to identify as a single interface. We focus on the thickness of the shear band because of the transition zone between the bulk and gouge materials. The transition zone can have various thickness ranging from 0 to 1 mm (see Figure 4). Because of this transition zone, a prediction only from thin section observations, of the morphology of the rupture surface which will appear after opening the broken sample, is not possible.

[61] Quantitative measurement of roughness and gouge show scaling invariance. Fracture roughness is shown to be correctly described over up to 3 orders of magnitude by a self-affine geometry with a roughness exponent ζ, varying from 0.7 to 0.78. The gouge granulometry appears to be power law distributed, with an exponent, *e*, varying from 1.44 to 1.91. We observed the influence of both confining pressure and shearing displacement on these two exponents. The *e* exponent appears to increase with the shearing displacement and the confining pressure. This shows that a grain fracturing process is acting within the gouge during the deformation. For low confining pressure, ζ decreases with the shearing, and indicates a roughening of the surface. On the contrary, for high confining pressure ζ increases with the shearing, indicating a smoothing of the surface. These results show a complex coupling between the fault gouge and fault roughness. The shear band deformation involves both gouge and roughness evolution during the shearing. The coupling between gouge and roughness appears to be pressure dependent.

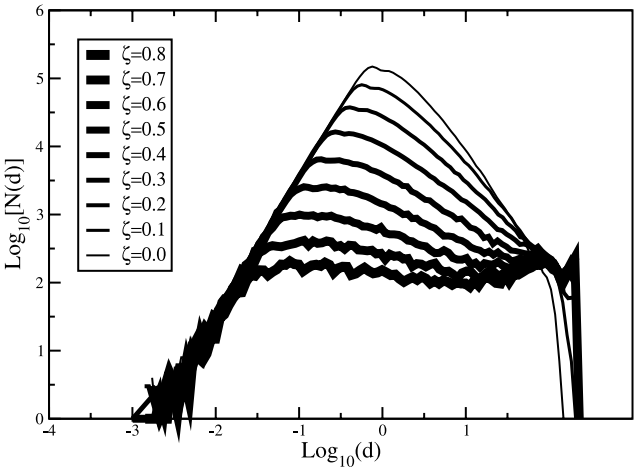

Figure 17. Particle size distribution from a geometric model where particles are created from the evolution of the roughness exponent of synthetic surfaces. Excess areas are responsible for the new particle creation. Particle size is obtained from the square root of the area.

These processes should be taken into account in constitutive laws for the mechanical behavior of the interface.

[62] **Acknowledgments.** We thanks S. Roux for helpful comments, A. M. Boullier for her help in thin section observation, and D. Hantz and Y. Orengo for technical support.

References

Amitrano, D., Emission acoustique des roches et endommagement: Approches experimentale et numerique, Application a la sismicite miniere, Ph.D. thesis, Univ. Joseph Fourier, Grenoble, France, 1999.

Amitrano, D., and D. Hantz, Acoustic emission of jointed and intact rocks during triaxial compression test, in *Proceedings of the International Conference on Mechanics of Jointed and Faulted Rock*, edited by H. P. Rossmanith, pp. 375–380, A. A. Balkema, Brookfield, Vt., 1998.

Atkinson, B., *Fracture Mechanics of Rock*, Academic, San Diego, Calif., 1991.

Barton, N., and V. Choubey, The shear strength of rock joints in theory and practice, *Rock Mech.*, *10*, 1–54, 1977.

Belem, T., F. Homand, and M. Souley, Quantitative parameters for rock joint surface roughness, *Rock Mech. Rock Eng.*, *33*, 217–242, 2000.

Besuelle, P., Compacting and dilating shear bands in porous rock: Theoretical and experimental conditions., *J. Geophys. Res.*, *106*, 13,435–13,442, 2001.

Biarez, J., and P.-Y. Hicher, Influence de la granulometrie et de son evolution par rupture de grains sur le comportement mcanique des materiaux granulaires, *Rev. Fr. Genie Civ.*, *1*(4), 607–631, 1997.

Blenkinsop, T., and T. Fernandes, Fractal characterization of particle size distributions in chrominites from the Great Dyke Zimbabwe, *Pure Appl. Geophys.*, *157*, 505–521, 2000.

Boffa, J., C. Allain, and J. Hulin, Experimental analysis of fracture rugosity in granular and compact rocks, *Eur. Phys. J. Appl. Phys.*, *2*(3), 281–289, 1998.

Bouchaud, E., Scaling properties of cracks, *J. Phys. Condens. Matter*, *9*, 4319–4344, 1997.

Bouchaud, E., G. Lapasset, and J. Planès, Fractal dimension of fractured surfaces: A universal value?, *Europhys. Lett.*, *13*, 73–79, 1990.

Brace, W., B. Paulding, and C. Scholz, Dilatancy in the fracture of crystalline rocks, *J. Geophys. Res.*, *71*, 3939–3953, 1966.

Brown, S., and C. Scholz, Broad bandwith study of the topography of natural rock surface, *J. Geophys. Res.*, *90*, 12,575–12,582, 1985.

Costin, L., A microcrack model for the deformation and failure of brittle rock, *J. Geophys. Res.*, *88*, 9485–9492, 1983.

Cox, B. L., and J. S. Y. Wang, Fractal surfaces: Measurement and application in earth sciences, *Fractals*, *1*, 87–115, 1993.

Dieterich, J. H., Modeling of rock friction, 1, Experimental results and constitutive equations, *J. Geophys. Res.*, *84*, 2161–2168, 1979.

Falconer, K. J., *Fractal Geometry: Mathemathical Foundations and Applications*, John Wiley, New York, 1990.

Feder, J., *Fractals*, Plenum, New York, 1988.

Gao, H., and J. Rice, Shear-stress intensity factors for a planar crack with slightly curved front, *J. Appl. Mech.*, *53*(4), 774–778, 1986.

Gao, H., J. Rice, and J. Lee, Penetration of a quasi-statically slipping crack into a seismogenic zone of heterogeneous fracture-resistance, *J. Geophys. Res.*, *96*, 21,535–21,548, 1991.

Hecht, C., Appolonian packing and fractal shape of grains improving geomechanical properties in engineering geology, *Pure Appl. Geophys.*, *157*, 487–504, 2000.

Hirata, T., T. Satoh, and K. Ito, Fractal structure of spacial distribution of microfracturing in rock, *Geophys. J. R. Astron. Soc.*, *90*, 369–374, 1987.

Hoek, E., Strength of jointed rock masses, *Geotechnique*, *33*(3), 187–223, 1983.

Homand, F., T. Belem, and M. Souley, Friction and degradation of rock joint surface under shear loads, *Int. J. Numer. Anal. Methods Geomech.*, *25*(1), 1–27, 2001.

Jaeger, J. C., and N. G. W. Cook, *Fundamentals of Rock Mechanics*, Chapman and Hall, New York, 1979.

Karner, S., and C. Marone, The effect of shear load on frictional healing in simulated fault gouge, *Geophys. Res. Lett.*, *25*(24), 4561–4564, 1998.

Keller, J., S. Hall, and K. McClay, Shear fracture pattern and microstructural evolution in transpressional fault zones from field and laboratory studies, *J. Struct. Geol.*, *19*(9), 1173–1187, 1997.

King, G., and C. Sammis, The mechanims of finite brittle strain, *Pure Appl. Geophys.*, *138*(4), 611–640, 1992.

Kranz, R., Microcracks in rocks: A review, *Tectonophysics*, *100*, 449–480, 1983.

Lahaie, F., Pertinence du formalisme des transitions de phase pour aborder la mecanique des objets geologiques, Ph. D. these, Univ. Joseph Fourier, Grenoble, France, 2000.

Lin, A., S-C cataclasite in granitic rock, *Tectonophysics*, *304*, 257–273, 1999.

Lockner, D., and J. Byerlee, Precursory AE patterns leading to rock fracture, in P*roceedings of the Vth Conference on Acoustic Emission/ Microseismic Activity in Geologic Structures and Materials*, edited by H. R. Hardy, pp. 45–58, Trans Tech, Clausthal-Zellerfeld, Germany, 1991.

Lockner, D., J. Byerlee, V. Kuskenko, A. Ponomarev, and A. Sidorin, Quasi-static fault growth and shear fracture energy in granite, *Nature*, *350*, 39–42, 1991.

Lopez, J., and J. Schmittbuhl, Anomalous scaling of fracture surfaces, *Phys. Rev. E*, *57*, 6405–6406, 1998.

Mair, K., I. Main, and S. Elphick, Sequential growth of deformation bands in the laboratory, *J. Struct. Geol.*, *22*, 25–42, 2000.

Mair, K., S. Elphick, and I. Main, Influence of confining pressure on the mechanical and structural evolution of laboratory deformation bands, *Geophys. Res. Lett.*, *29*(10), 1410, doi:10.1029/2001GL013964, 2002.

Måløy, K. J., A. Hansen, E. L. Hinrichsen, and S. Roux, Experimental measurements of the roughness of brittle cracks, *Phys. Rev. Lett.*, *68*, 213–215, 1992.

Mandelbrot, B. B., D. E. Passoja, and A. J. Paullay, Fractal character of fracture surfaces of metals, *Nature*, *308*, 721–722, 1984.

Marone, C., Laboratory-derived friction laws and their application to seismic faulting, *Annu. Rev. Earth Planet. Sci.*, *26*, 643–696, 1998.

Marone, C., and C. Scholz, Particle-size distributions and microstructures within simulated fault gouge, *J. Struct. Geol.*, *11*(7), 799–814, 1989.

Mehrabi, A., H. Rassamdana, and M. Sahimi, Characterization of long-range correlations in complex distributions and profiles, *Phys. Rev. E*, *56*(1), 712–722, 1997.

Menendez, B., W. Zhu, and T.-F. Wong, Micromechanics of brittle faulting and cataclastic flow in Berea Sandstone, *J. Struct. Geol.*, *18*(1), 1–16, 1996.

Michibayashi, K., The role of intragranular fracturing on grain size reduction in feldspar during mylonitization, *J. Struct. Geol.*, *18*(1), 17–25, 1996.

Moore, D., R. Summers, and J. Byerlee, Sliding behavior and deformation textures of heated illite gouge, *J. Struct. Geol.*, *11*(3), 329–342, 1989.

Power, W., Topography of natural and artificial fractures in granite rocks: Implications for studies of rock friction and fluid migration, *Int. J. Rock Mech. Min. Sci.*, *34*, 979–989, 1997.

Power, W. L., T. E. Tullis, S. R. Brown, G. N. Boitnott, and C. H. Scholz, Roughness of natural fault surfaces, *Geophys. Res. Lett.*, *14*, 29–32, 1987.

Press, W. H., S. A. Teukolsky, W. T. Vetterling, and B. P. Flannery, *Numerical Recipies*, Cambridge Univ. Press, New York, 1992.

Reches, Z., and D. Lockner, Nucleation and growth of faults in brittle rocks, *J. Geophys. Res.*, *99*, 18,159–18,173, 1994.

Ruina, A., Slip instability and state variables friction laws, *J. Geophys. Res.*, *88*, 10,359–10,370, 1983.

Sakellariou, M., B. Nakos, and C. Mitsakaki, Technicale note: On the fractal character of rock surfaces, *Int. J. Rock Mech. Min. Sci. Geomech. Abstr.*, *28*(6), 527–533, 1991.

Sammis, C., and R. L. Biegel, Fractals, fault-gouge, and friction, *Pure Appl. Geophys.*, *131*(1/2), 255–271, 1989.

Savage, J., J. Byerlee, and D. Lockner, Is internal friction friction, *Geophys. Res. Lett.*, *23*, 487–490, 1996.

Schmittbuhl, J., S. Gentier, and S. Roux, Field measurements of the roughness of fault surfaces, *Geophys. Res. Lett.*, *20*, 639–641, 1993.

Schmittbuhl, J., J. Vilotte, and S. Roux, Reliability of self-affine measurements, *Phys. Rev. E*, *51*, 131–147, 1995a.

Schmittbuhl, J., F. Schmitt, and C. Scholz, Scaling invariance of crack surfaces, *J. Geophys. Res.*, *100*, 5953–5973, 1995b.

Schmittbuhl, J., A. Delaplace, K. Maloy, H. Perfettini, and J. Vilotte, Slow crack propagation and slip correlations, *Pure Appl. Geophys*, in press, 2002.

Scholz, H., *The Mechanics of Earthquakes and Faulting*, Cambridge Univ. Press, New York, 1990.

Schulson, E., D. Illiescu, and C. Renshaw, On the initiation of shear faults during brittle compressive failure: A new mechanism, *J. Geophys. Res.*, *104*, 695–705, 1999.

Simonsen, I., A. Hansen, and O. M. Nes, Using wavelet transforms for hurst exponent determination, *Phys. Rev. E*, *58*, 2779, 1998.

Sleep, N., E. Richardson, and C. Marone, Physics of friction and strain rate localization in synthetic fault gouge, *J. Geophys. Res.*, *105*, 25,875–25,890, 2000.

Suteanu, C., D. Zugravescu, and F. Munteanu, Fractal approach of structuring by fragmentation, *Pure Appl. Geophys.*, *157*, 539–557, 2000.

Turcotte, D. L., *Fractals and Chaos in Geology and Geophysics*, Cambridge Univ. Press, New York, 1992.

Velde, B., D. Moore, A. Badri, and B. Ledesert, Fractal analysis of fractures during brittle to ductile changes, *J. Geophys. Res.*, *98*, 11,935–11,940, 1993.

Wang, W., and C. Scholz, Wear processes during frictionnal sliding of rocks: A theoretical and experimental study, *J. Geophys. Res.*, *99*, 6789–6799, 1994.

Weiss, J., and M. Gay, Fracturing of ice under compression creep as revealed by a multifractal analysis, *J. Geophys. Res.*, *103*, 24,005–24,016, 1998.

Wibberley, C., J.-P. Petit, and T. Rives, Micromechanics of shear rupture and the control of normal stress, *J. Struct. Geol.*, *22*, 411–427, 2000.

Yang, Z., and S. Lo, An index for describing the anisotropy of joint surfaces, *Int. J. Rock Mech. Min. Sci.*, *34*, 1031–1044, 1997.

Yu, X., and B. Vayssade, Joint profiles and their roughness parameters, *Int. J. Rock Mech. Min. Sci. Geomech. Abstr.*, *28*(4), 333–336, 1991.

D. Amitrano, Laboratoire Environnement Géomécanique et Ouvrages, Ecole Nationale Supérieure des Mines de Nancy, Parc de Saurupt, 54042, Nancy Cedex, France. (amitrano@mines.u-nancy.fr)

J. Schmittbuhl, Laboratoire de Géologie, Ecole Normale Supérieure de Paris, 24 rue Lhomond, 75231 Paris Cedex 05, France. (Jean.Schmittbuhl@ens.fr)